

Interface-tuning of ferroelectricity and quadruple-well state in CuInP_2S_6 via ferroelectric oxide

Kun Wang¹, Du Li², Jia Wang¹, Yifei Hao¹, Hailey Anderson¹, Li Yang², Xia Hong^{1*}

¹ *Department of Physics and Astronomy & Nebraska Center for Materials and Nanoscience, University of Nebraska-Lincoln, Lincoln, Nebraska 68588-0299, USA.*

² *Department of Physics, Washington University in St. Louis, St. Louis, Missouri 63130-4899, USA.*

*Email: xia.hong@unl.edu

KEYWORDS: CuInP_2S_6 , $\text{Pb}(\text{Zr,Ti})\text{O}_3$, ferroelectricity, piezoelectricity, interface tuning, piezoresponse force microscopy

ABSTRACT

Ferroelectric van der Waals CuInP_2S_6 possesses intriguing quadruple-well states and negative piezoelectricity. Its technological implementation has been impeded by the relatively low Curie temperature (bulk $T_C \sim 42^\circ\text{C}$) and the lack of precise domain control. Here we show that CuInP_2S_6 can be immune to the finite size effect and exhibits enhanced ferroelectricity, piezoelectricity, and polar alignment in the ultrathin limit when interfaced with ferroelectric oxide $\text{PbZr}_{0.2}\text{Ti}_{0.8}\text{O}_3$ films. Piezoresponse force microscopy studies reveal that the polar domains in thin CuInP_2S_6 fully conform to those of underlying $\text{PbZr}_{0.2}\text{Ti}_{0.8}\text{O}_3$, where the piezoelectric coefficient changes sign and increases sharply with reducing thickness. High temperature *in situ* domain imaging points to

a significantly enhanced T_C exceeding 200 °C for 13 nm CuInP₂S₆ on PbZr_{0.2}Ti_{0.8}O₃. Density functional theory modeling and Monte Carlo simulations show that the enhanced polar alignment and T_C can be attributed to interface-mediated structure distortion in CuInP₂S₆. Our study provides an effective material strategy to engineer the polar properties of CuInP₂S₆ for flexible nanoelectronic, optoelectronic, and mechanical applications.

Layered van der Waals (vdW) ferroelectric CuInP₂S₆ (CIPS) hosts unconventional quadruple-well energy¹ and high ionic conductivity,^{2, 3} which lead to various exotic phenomena, including negative piezoelectric coefficient,⁴ thickness-dependent in-plane polarization,⁵ giant electrostriction enabled strain tunability,⁶ strong coupling of ferroelectric polarization with ionic migration and topography variation,⁷⁻⁹ and the self-rectifying memristor effect.¹⁰ Compared with other vdW ferroelectric semiconductors, the above room temperature Curie temperature (bulk $T_C \sim 42$ °C),¹¹ large band gap ($E_g \sim 2.9$ eV),¹² and large out-of-plane polarization ($P \sim 4$ μC/cm²)⁴ make CIPS the most promising candidate for developing flexible and transparent nanoelectronic and optoelectronic devices, such as nonvolatile memory,^{11, 13, 14} negative capacitance transistors,^{15, 16} memristors,^{10, 17} rectifiers,^{10, 18} photocatalysis,¹⁹ and photovoltaics.²⁰

In CIPS, the ferroelectric polarization mainly originates from the off-center displacement of Cu in the sulfur frames. Due to the mobile Cu ions, the ferroelectric order parameter is highly susceptible to thermal,^{7, 21} electrical,² and mechanical stimulations.^{9, 22} It has been shown that domain writing in CIPS always yields diffusive, rough domain walls (DWs), precluding precise polarization control at the nanoscale.^{5, 13} The relatively low T_C and lack of domain control in CIPS can compromise the thermal stability and density of polarization-enabled device applications. To transcend these material limitations, it calls for an effective strategy to promote the polar alignment

in CIPS. A promising route is to interface CIPS with a ferroelectric with well-controlled polar states. For example, enhanced piezoelectric response has previously been observed in organolead trihalide thin films prepared on ferroelectric oxide films, where the interfacial coupling aligns the polar liquid state in the hybrid perovskite.²³

In this study, we report controlled domain formation and enhanced piezoelectricity and ferroelectricity in thin CIPS flakes interfaced with epitaxial ferroelectric $\text{PbZr}_{0.2}\text{Ti}_{0.8}\text{O}_3$ (PZT) films. Piezoresponse force microscopy (PFM) studies show that thin CIPS flakes fully mirror the domain structures of underlying PZT, in contrast to the spontaneously formed mosaic domains observed in flakes prepared on doped Si and Au base layers. The enhanced polar alignment for thin CIPS on PZT is accompanied by a sign change in piezoelectric coefficient d_{33} , which increases sharply from 5.2 to 14.8 pm/V as the flake thickness t_{CIPS} is reduced from 21 to 6 nm. Density functional theory (DFT) modeling of CIPS/ PbTiO_3 (PTO) reveals interface-mediated structure distortion in CIPS, which favors the polarization of CIPS to be antialigned with that of PZT. *In situ* domain imaging via high temperature PFM further shows that T_C in thin CIPS is enhanced to above 200 °C, which becomes comparable to that of technologically important ferroelectric polymers²⁴ and lead-free oxide ceramics.^{25, 26} The interface-lattice-coupling-enabled T_C enhancement is corroborated by Monte Carlo simulations. Details on the sample preparation, PFM characterizations, and theoretical modeling are provided in Methods. All experiments are conducted at room temperature unless otherwise specified.

RESULTS AND DISCUSSION

Domain formation in CIPS

We transfer mechanically exfoliated 8-300 nm CIPS flakes on 50 nm epitaxial (001) PZT films (Figure 1a) with pre-patterned domain structures and compare their PFM response with those

prepared on doped Si and Au base layers (See Methods). The PZT films are deposited on 10 nm $\text{La}_{0.67}\text{Sr}_{0.33}\text{MnO}_3$ (LSMO) buffered SrTiO_3 (STO) substrates and possess out-of-plane polarization (Figure S1a and S2). Figure 1b shows the PFM amplitude and phase response of a bare PZT film versus the bias voltage (V_{bias}) with respect to the bottom electrode. The coercive voltages for the polarization up (P_{up}) and down (P_{down}) states are -1.15 V and 1.25 V, respectively. Atomic force microscopy (AFM) studies show that all three types of base layers possess smooth surfaces with typical root mean square roughness of $\leq 5 \text{ \AA}$ (Figure S1b-d).

Figure 1c-d shows the PFM phase and amplitude images, respectively, taken on a 13-14 nm CIPS flake (Figure S3a) transferred on a PZT film pre-patterned into the P_{up} state. The CIPS flake exhibits a uniform domain structure, with the phase signal comparable with that of PZT. This is in sharp contrast to the samples prepared on doped Si (Figure 1e-f) and Au (Figure 1g-h) base layers, where CIPS flakes of the same thickness (14 nm, Figure S3b-c) show spontaneously formed long-stripe domains with characteristic widths on the order of 100 nm. The distinct domain structures suggest that the PZT base layer promotes the alignment of polarization in CIPS.

To assess the length scale of the interaction between CIPS and PZT, we pre-pattern on three PZT films a series of rectangular P_{down} domains in a uniformly polarized P_{up} background (Figure 2a) and transfer CIPS flakes of various thicknesses on top (Figure 2b-d, and Figure S4-6), denoted as samples S1-S3. The 13 nm (Figure 2c) and 15 nm CIPS flakes (Figure 2d) form the same domain pattern as that of underlying PZT. For the 18 nm CIPS (Figure 2d), the PFM response on top of the P_{up} domains of PZT is uniform and in phase with that of PZT, while local phase variations start to emerge in the region on top of the P_{down} domains of PZT. The polarization asymmetry is clearly manifested in the 26 nm CIPS, where spontaneous stripe domains similar to those observed in Figure 1e-f only show up in the region on top of the P_{down} domains of PZT. For the 28 nm flake,

in contrast, the stripe domain structures form on top of both the P_{down} and P_{up} domains of PZT. For the 55 nm and thicker flakes (Figure 2c), the domain distribution is no longer correlated with the underlying PZT polarization. The evolution of domain structure with t_{CIPS} suggests that the mechanism aligning the polarization between CIPS and PZT occurs at the interface and decays with increasing t_{CIPS} . The different domain patterns in the intermediate thickness range (18 nm and 26 nm) also show that the P_{up} state has a slightly larger critical thickness for the transition to bulk-like behavior, inferring that the CIPS polarization can be more effectively aligned by the P_{up} state of PZT than the P_{down} state.

Enhanced d_{33} in thin CIPS on PZT

For the 14 nm CIPS/PZT stack, the overall piezoresponse is homogeneous and in phase with that of bare PZT (Figure 1c), while its amplitude is weaker (Figure 1d). We carry out off-resonance PFM ramping measurements to quantify the piezoelectric coefficient d_{33} (see Methods). Figure 3a shows the PFM ramping curves taken on the three CIPS samples shown in Figure 1c-h, where the amplitude signal of all samples exhibits a linear V_{bias} -dependence above the instrument signal floor (~ 0.5 mV). From the slope, we obtain an effective piezoelectric coefficient d_{33}^{tot} of 3.9 pm/V for the CIPS/PZT stack (see Methods). This is much smaller than that of PZT $d_{33}^{\text{PZT}} = 39 \pm 2$ pm/V, consistent with the PFM amplitude image (Figure 1d). Since both CIPS and PZT layers contribute to the piezoelectric response, the net piezoresponse is given by:

$$d_{33}^{\text{tot}} = \nu_{\text{PZT}} \cdot d_{33}^{\text{PZT}} \pm \nu_{\text{CIPS}} \cdot d_{33}^{\text{CIPS}}, \quad (1)$$

where ν_{PZT} and ν_{CIPS} are the fractional bias voltage dropped across the PZT and CIPS layers, respectively. The positive (negative) sign applies to the condition that the polarization directions of CIPS and PZT are aligned (antialigned). We then perform finite element analysis to model the voltage distribution (see Methods). Figure 3b-c shows the simulated result for a 14 nm CIPS/50

nm PZT stack assuming dielectric constants of 52 for CIPS¹³ and 100 for PZT,²⁷ which yields $\nu_{\text{PZT}} = 0.26$ and $\nu_{\text{CIPS}} = 0.74$. The corresponding piezoelectric response from the PZT layer is $\nu_{\text{PZT}} \cdot d_{33}^{\text{PZT}} = 10.1$ pm/V. Using Eq. (1), we deduce the piezoelectric response from CIPS to be -6.2 pm/V. The overall phase of the piezoelectric response for the stack is thus determined by the PZT layer.

Since CIPS has the unconventional quadruple-well ferroelectric states,¹ there are two possible configurations for the polarization of CIPS that lead to the negative piezoelectric response: 1) the polarization is aligned with that of PZT, while d_{33}^{CIPS} is negative; 2) the polarization is antialigned with that of PZT, while d_{33}^{CIPS} is positive. To determine which scenario applies to our system, we perform DFT calculations for a CIPS/PTO heterostructure as a model system (see Methods). Figure 3e-f shows the calculated crystal structures of fully relaxed CIPS on a frozen PTO substrate, with the polarization of PTO fixed in the P_{down} state. We calculate the total energy of the heterostructure with the polarization of CIPS in either the P_{up} (Figure 3e) or the P_{down} state (Figure 3f). The energy of the antialigned configuration is 25 meV lower than that of the aligned configuration (Figure S17). This energy difference can be associated with the lattice distortion of the interfacial CIPS due to the strain imposed by PTO, as revealed by the DFT calculations. For the P_{up} state of CIPS (polarizations antialigned with PZT), all copper ions in the interfacial layer of CIPS lie in the same horizontal plane. In contrast, for the P_{down} state (polarization aligned with PZT), there is a larger variation in Cu ion position, causing higher lattice distortion (Figure S18). The standard deviations of the z -direction Cu displacement are 0.01 Å and 0.15 Å for the P_{up} and P_{down} states of CIPS, respectively. This strain-mediated lattice distortion results in a higher elastic energy cost for the P_{down} state of CIPS, which can account for the preference for antialigned polarization between CIPS and PTO.

Based on this result, we adopt the negative sign in Eq. (1) and obtain a positive d_{33}^{CIPS} of 8.5 pm/V for the 14 nm CIPS on PZT. As a control study, we also quantify d_{33}^{CIPS} for CIPS on Si and Au base layers. To determine the sign of d_{33}^{CIPS} , we conduct PFM switching measurements and compare the hysteresis loops with that obtained on bare PZT (Figure S9). The phase switching hysteresis of CIPS on Si and Au is in counterclockwise direction, opposite to that obtained on PZT. We thus conclude d_{33}^{CIPS} for CIPS on Si and Au is negative, which is consistent with previous reports.^{1,4} Figure 3d compares the d_{33}^{CIPS} values averaged over different spots for the 14 nm CIPS flakes on PZT, Si, and Au base layers. Compared with the results obtained on CIPS flakes on Si (-2.2±0.2 pm/V) and Au (-1.8±0.2 pm/V), d_{33} for CIPS on PZT (8.0±0.7 pm/V) is not only significantly higher but also changes sign.

The positive d_{33}^{CIPS} for CIPS on PZT reflects a change in the free energy profile, which can be attributed to the interfacial strain imposed by PZT. For standalone CIPS (Figure 3g), the displacements of Cu for the P_{up} (+) and P_{down} (-) states are symmetric and within the vdW layer. When the flake is subjected to an external electric field, the change of the interlayer vdW gap is larger than that of the intralayer separation while in the opposite direction, leading to a negative d_{33}^{CIPS} in the ground state (GS).⁴ In the metastable state (MS), the Cu ion is further displaced and enters the gap between the neighboring vdW layers, leading to a positive d_{33}^{CIPS} . Even though the metastable state energy is lower relative to the ground state, it corresponds to a larger Cu displacement that requires overcoming a slight energy barrier. As a result, a negative d_{33}^{CIPS} is commonly observed in standalone CIPS. On the other hand, for CIPS on PTO in the P_{down} state, the strain induced by PTO shifts the lower sulfur ion position towards the Cu ion (Figure 3h). Such distortion leads to a higher elastic energy for the P_{down} state of CIPS, effectively tilting the quadruple well energy profile. This change not only favors the P_{up} state, or antialigned polarization

between CIPS and PTO, but also suppresses the energy barrier between the +GS and +MS state, making the metastable state accessible. This scenario naturally explains the positive d_{33}^{CIPS} observed in thin CIPS on PZT. Such strain modulation is consistent with previous reports of CIPS.^{1, 6, 22} Similar interfacial strain-mediated polarization asymmetry has been widely observed in epitaxial ferroelectric oxide heterostructures.²⁸

Thickness dependence of d_{33}^{CIPS}

We systematically examine the piezoelectric response of CIPS flakes in a wide thickness range (8-300 nm) on the three types of base layers (Figure 4). For control samples on Au and Si base layers, d_{33}^{CIPS} remains negative for the entire thickness range. The value is about -10 pm/V for thick flakes (> 100 nm) and gradually decreases with reducing t_{CIPS} , reaching about -1 pm/V for 6 nm CIPS on Si and -1.6 pm/V for 13 nm CIPS on Au. The suppression of d_{33}^{CIPS} in thin CIPS has been reported previously^{29, 30} and can be attributed to the finite size effect due to the enhanced depolarization in thin ferroelectrics.³¹

In contrast, CIPS on PZT shows an unconventional t_{CIPS} -dependence of d_{33}^{CIPS} , which can be divided into three distinct regions. For thick flakes (Region I: $t_{\text{CIPS}} > 50$ nm), d_{33}^{CIPS} is about -10 pm/V and does not show apparent thickness dependence, similar to the behavior of thick flakes on Au and Si. In the intermediate thickness region (Region II: $25 \text{ nm} < t_{\text{CIPS}} < 50$ nm), there is a significant variation in the d_{33}^{CIPS} values, with both positive and negative d_{33}^{CIPS} observed. For example, d_{33}^{CIPS} extracted on 26 nm CIPS flakes varies from 4.9 pm/V to -11.9 pm/V. For thin flakes (Region III: $t_{\text{CIPS}} < 25$ nm), d_{33}^{CIPS} becomes positive and exhibits a monotonical increase with decreasing t_{CIPS} , changing from 5.2 pm/V for 21 nm flake to 14.8 pm/V for 6 nm flake. This result is opposite to the thickness dependence observed in the CIPS samples on Au and Si.

Our result shows that CIPS on PZT is not subjected to the finite size effect. This can also be

understood within the scenario of the tilted energy quadruple-well of the interfacial CIPS due to the structure distortion. When CIPS is settled in the metastable state, it corresponds to a larger displacement of the Cu ions, which produces an enhanced, positive d_{33}^{CIPS} . Such structural distortion is mediated by the interface lattice coupling with PZT and thus short-ranged, settling the interfacial layers in the metastable state. For the CIPS layers away from the interface, the strain is relaxed and d_{33}^{CIPS} gradually recovers the bulk behavior. The overall piezoresponse of a CIPS sample is determined by the net effect of the strained interfacial layers in the metastable state ($d_{33}^{\text{MS}} > 0$) and the relaxed layers in the ground state ($d_{33}^{\text{GS}} < 0$), which can be described by $d_{33}^{\text{CIPS}} = \nu_{\text{MS}} \cdot d_{33}^{\text{MS}} + \nu_{\text{GS}} \cdot d_{33}^{\text{GS}}$, with ν_{MS} and ν_{GS} the fractional bias voltage across the layers in the metastable and ground states, respectively. With increasing t_{CIPS} , the relaxed layers account for a larger fraction across the sample, leading to a larger ν_{GS} . As a result, the measured d_{33}^{CIPS} shows a continuous, monotonic decrease with increasing t_{CIPS} , as observed in Region III. Since strain relaxation can be affected by local boundary conditions and defect states, the critical layer number for the transition from the metastable state to the ground state can vary from sample to sample, which accounts for the large variation in the magnitude and even the sign of d_{33}^{CIPS} for CIPS on PZT in Region II. When t_{CIPS} is further increased to Region I, CIPS layers in the ground state dominate the piezoelectric response, and the net d_{33} becomes negative (Region I). We emphasize that consistent thickness-dependences for the evolution of domain structures (Figure 2 and Figure S5) and d_{33}^{CIPS} (Figure 4) have been observed in multiple samples with various CIPS sizes and thicknesses, including isolated flakes with uniform thickness and large flakes with a thickness distribution. It is conceivable that the flakes with different sizes and thickness distributions may be subjected to slight variation in mechanical conditions during the exfoliation and transfer procedure. The fact that we observe highly reproducible PFM results clearly demonstrates that the

interface-mediated effect is robust and universal.

Enhanced Curie Temperature for CIPS

As the structure distortion in CIPS modifies the ferroelectric free energy profile, it also affects T_C . To quantify this effect, we perform *in situ* PFM imaging on sample S1 (Figure 2c) at elevated temperatures (up to 225 °C, see Methods), which are well below the T_C of epitaxial PZT thin films.²⁸ As shown in Figure 5a-c, the P_{up} and P_{down} domains in bare PZT remain stable over the entire thermal cycle. This helps us establish the baseline for assessing the thermal evolution of domain structures in CIPS, which excludes any influence from the change of underlying PZT.

Figure 5a shows the *in situ* PFM phase images at selected temperatures taken on the 13 nm region of CIPS, which belongs to Region III. From 20 °C to 175 °C, the domain structure in CIPS fully conforms to that of the underneath PZT and does not show appreciable change, even though this temperature well exceeds the T_C of bulk CIPS (~42 °C).¹¹ Small bubble domains start to emerge at 200 °C (Figure 5b), clearly illustrating that the sample is approaching T_C . At 225 °C, the CIPS-covered region exhibits noisy PFM responses, the domain structure becomes blurred, and the phase contrast between regions on top of the P_{up} and P_{down} domains of PZT is uniformly suppressed. Similarly, the *in situ* PFM amplitude images (Figure S16a) show that the DWs in the CIPS region are clearly recognizable below 200 °C and disappear at 225 °C. We thus conclude that the T_C for the 13 nm CIPS is between 200 °C and 225 °C ($T_C \approx 485 \pm 12$ K), which is about 54% higher than the bulk value. After the sample is cooled back down to 20 °C, the PZT domain structures re-emerge in the CIPS region, indicating that the polar alignment between CIPS and PZT is recovered after the thermal cycle. For comparison, we also perform *in situ* PFM on 14 nm CIPS on Si and Au base layers (Figure S12-15). The results show that the T_C for the CIPS on Si and Au are between 50 °C and 60 °C, which is consistent with previous reports for CIPS flakes

and close to the bulk value.²⁹ It is important to note that the enhanced T_C in thin CIPS exceeds the values for ferroelectric polymer P(VDF-TrFE)²⁴ and oxide BaTiO₃,²⁵ and approaches that of SrBi₂Ta₂O₉,²⁶ which makes CIPS highly competitive for developing wearable nanoelectronic and optoelectronic applications.

Figure 5c shows *in situ* PFM phase images at selected temperatures taken on the 55 nm region of CIPS on PZT, which belongs to Region I. At 20 °C, CIPS exhibits randomly distributed domain structures. When heated to 100 °C, these domains disappear and the overall PFM phase signals become uniformly blurred and noisy, similar to those for the 13 nm region at 225 °C. The PFM amplitude signal of DWs is clearly recognizable at 20 °C and becomes fuzzy when heated to 100 °C (Figure S16b). These results suggest that the 55 nm CIPS flake is already heated above T_C . After cooling down to 20 °C, new random domains emerge, which are different from those before heating, further confirming that the sample has been cycled through T_C .³² This result demonstrates that the T_C enhancement is confined to thin CIPS flakes.

To understand the effect of lattice distortion on T_C , we employ the Nudged Elastic Band (NEB) method to calculate the ferroelectric energy barriers for CIPS (see Methods and Supporting Information Section 7). The results reveal an increased energy barrier from 214 meV to 374 meV after setting CIPS on PTO. Fitting the double well energy using the Landau theory shows that the coefficients for the Landau energy expansion correspond to a T_C enhancement of 42%^{33, 34} (Supporting Information Section 7). The higher order terms induced by anharmonic couplings³⁵ may be considered in the future to give a more accurate description of the energy profile, but these terms will not significantly affect the variation of energy barrier induced by PTO. We further perform Monte Carlo simulations of the mean position of Cu in CIPS as a function of temperature (Figure 5d) and set T_C as the temperature at which the mean position of Cu approaches zero. We

extract T_c of 400 K for standalone CIPS and 650 K for CIPS on PTO, corresponding to a T_c enhancement of 63%. Considering the slight difference in crystal structures for PTO and PZT, we find the DFT modeling and Monte Carlo simulation results are in reasonable agreement with the experimental result.

CONCLUSIONS

In summary, we report controlled domain formation, enhanced ferroelectricity, and tunable piezoelectricity in thin CIPS interfaced with PZT. CIPS polarization is antialigned to that of PZT as the flake thickness is reduced below 25 nm. Thin CIPS flakes on PZT exhibit positive d_{33}^{CIPS} , which increases with decreasing t_{CIPS} , and an enhanced $T_c > 200$ °C. DFT modeling and Monte Carlo simulations reveal the critical role of interface-mediated lattice coupling in modifying the ferroelectric free energy. Our study provides an effective material strategy to precisely control domain formation and engineer ferroelectricity and piezoelectricity in CIPS, facilitating its implementation in flexible nanoelectronic, optoelectronic, and mechanical applications.

METHODS

Sample preparation

We deposit epitaxial (001) 50 nm PZT/10 nm LSMO heterostructures on STO substrates using off-axis radio frequency magnetron sputtering. The growth conditions can be found in Ref. ³⁶. X-ray diffraction θ - 2θ scans reveal that all PZT films are (001)-oriented with c -axis lattice constants of 4.17-4.18 Å (Figure S1), which is consistent with highly strained PZT films.²⁷ To prepare the Au base layer, we deposit 10 nm Au/2 nm Ti on a SiO₂ wafer (Novawafers[®]) using electron beam evaporation. We work with doped Si substrates (Novawafers[®]) with a resistivity of 1-5 mΩ cm.

We mechanically exfoliate CIPS flakes and transfer selected pieces on PZT, Si, and Au base layers using the dry transfer approach at ambient conditions. CIPS flakes are transferred on the pre-patterned domains in PZT after 24 hours of domain writing to ensure that the domain structures are stable and the surface electrostatic conditions are consistent before transfer (Supporting Information Section 5). All sample transfer procedures are conducted at room temperature.

Conductive AFM and PFM measurements

The conductive AFM and PFM measurements are carried out using a Bruker Multimode 8 AFM with conductive Pt/Ir-coated probes (Bruker SCM-PIT-V2). For domain writing, we apply a DC bias of ± 5 V to the AFM tip and ground the LSMO layer. The selected regions are first poled into the P_{up} state as a uniform background, within which the P_{down} domains are written.

The PFM imaging is conducted with an AC bias voltage close to one of the cantilever's resonant frequencies (310 ± 30 kHz). The driving bias amplitude for all PFM switching and imaging is 300 mV, lower than the coercive voltage of CIPS and PZT. The *in situ* PFM imaging is performed using Bruker's TAC Thermal Application Controller system. The samples are heated on the AFM sample holder and maintained at the target temperature for 30 minutes to achieve thermal equilibrium before imaging. For the PFM phase images shown in main text, the corresponding PFM amplitude images can be found in the Supporting Information.

To measure d_{33} , we perform off-resonance PFM ramping measurements. The applied bias is ramped at the sweeping rate of 0.1 V/s. We collect the PFM amplitude at a frequency of 40 kHz, which is well below the cantilever's free-space resonance frequency (~ 75 kHz). The PFM response is robust and frequency-independent at the frequency range of 20-60 kHz (Supporting Information Figure S7). The applied bias across CIPS and PZT layers is smaller than their coercive voltages in all measurements to avoid polarization switching. The magnitude of d_{33} of a sample is extracted

from the slope of PFM amplitude vs V_{bias} by the relation: $d_{33} = (S/I) \cdot (\partial A / \partial V_{\text{bias}})$. Here A is the output PFM amplitude, $S = 54 \text{ nm/V}$ is the tip deflection sensitivity, and $I = 16$ is the system vertical gain. As a control experiment, we characterize the piezoresponse of bare PZT and obtain an average value of $d_{33}^{\text{PZT}} = 39 \pm 2 \text{ pm/V}$, which is comparable with previously reported values for epitaxial PZT thin films.³⁷ We also perform PFM ramping measurements with different external DC bias superimposed on the AC bias³⁸ and obtain highly consistent results (Supporting Information Figure S8), confirming that the extracted d_{33} values are not affected by the surface electrostatic charges. More details of the PFM ramping measurement can be found in Supporting Information Section 3.

Each data point of d_{33} shown in Figure 4 is averaged over at least six locations in different regions/flakes with the same thickness. For each location, the measurements have been repeated at least twice to ensure the result is reproducible. For the temperature-dependent measurements (Figure 5), we have performed the *in-situ* PFM imaging twice following the same thermal cycling conditions and obtained consistent results.

Finite element analysis

We perform finite element analysis to model the bias voltage distribution across the CIPS/PZT stack. For our sample geometry, we assume a global ground provided by the LSMO layer and a point contact between the conductive AFM tip and the sample surface. Our analysis shows that the fraction of bias voltage across the CIPS layer (v_{CIPS}) varies from 0.62 to 0.97 as t_{CIPS} increases from 6 to 248 nm (Supporting Information Section 4).

DFT calculation

To obtain the ground state properties of CIPS/PTO interface, we construct the interface

supercell based on monolayer CIPS and four layers of PTO. A 2×3 supercell of PTO and a rectangular cell of CIPS are adopted for lattice match. PTO is compressed by 21% strain along a axis and 5% strain along b axis to compensate for lattice mismatch. The core electrons of atoms are eliminated by projector augmented-wave (PAW) potentials³⁹ as implemented in the Vienna *ab initio* simulation package (VASP).⁴⁰ The Perdew-Burke-Ernzerhof (PBE) function⁴¹ is used in the calculation and the spin-orbital coupling is not included. The energy cutoff is 400 eV for structure relaxation and solving the Kohn-Sham equation. We consider a Gamma point sampling in the reciprocal space of the supercell to get ground state energy. A vacuum distance of 15 Å between adjacent layers is used along the periodic direction to avoid spurious interactions. Despite the complexity of ferroelectric perovskite surface due to the interplay of lattice reconstruction,⁴² defect states,⁴³ and charged adsorbates,⁴⁴ as well as the anharmonic coupling between the Cu-In polar displacements and the structural distortions in CIPS,³⁵ our model focusing on the direct lattice coupling between CIPS and PbTiO₃ has successfully captured the enhanced T_c and polarization asymmetry in CIPS interfaced with PZT. Future theoretical efforts involving large-scale *ab initio* or force-field calculations⁴³ are required to fully account for the complex structural, chemical, and electrostatic interface conditions for this intriguing material system.

Monte Carlo simulation

In the Monte Carlo simulation,⁴⁵ the length of steps is set to 0.2 Å and the number of steps is 20000. We randomly pick up the direction (positive/negative along c direction) of each step with even probability. The acceptance is determined using the Metropolis Hastings algorithm.⁴⁵ This process is repeated about 50 times with a fixed starting point, and the average of final positions is used as the result. The entire process is repeated about 100 times to obtain the converged mean values.

ACKNOWLEDGMENTS

Funding: This work is primarily supported by the National Science Foundation (NSF) through Grant Number DMR-2118828 and EPSCoR RII Track-1: Emergent Quantum Materials and Technologies (EQUATE) Award No. OIA-2044049, and the Nebraska Center for Energy Sciences Research (NCESR). D. Li is supported by the NSF through Grant Number DMR-2118779. L. Yang is supported by the NSF through Grant Number DMR-2124934. The research is performed in part in the Nebraska Nanoscale Facility: National Nanotechnology Coordinated Infrastructure and the Nebraska Center for Materials and Nanoscience, which are supported by the National Science Foundation under Award No. ECCS: 2025298, and the Nebraska Research Initiative. The computational resources are provided by the Extreme Science and Engineering Discovery Environment (XSEDE), which is supported by NSF through Grant Number ACI-1548562. D. Li and L. Yang acknowledge the Texas Advanced Computing Center (TACC) at The University of Texas at Austin for providing HPC resources.

Author contributions: X. Hong and K. Wang conceive the project and design the experiments. X. Hong supervises the project. Y. Hao prepares the PZT thin films. K. Wang and Y. Hao carry out structural characterizations of PZT. K. Wang, J. Wang, and H. Anderson prepare the CIPS samples. K. Wang and J. Wang contribute to the conductive AFM and PFM studies. D. Li and L. Yang perform DFT calculations and Monte Carlo modeling. K. Wang and X. Hong write the manuscript. All authors contribute to the results discussion and manuscript preparation.

Notes: The authors declare no competing interests.

REFERENCES

- ¹ J. A. Brehm, S. M. Neumayer, L. Tao, A. O'Hara, M. Chyasnovich, M. A. Susner, M. A. McGuire, S. V. Kalinin, S. Jesse, and P. Ganesh, Tunable quadruple-well ferroelectric van der Waals crystals, *Nature Materials* **19**, 43 (2020).
- ² D. Zhang, Z.-D. Luo, Y. Yao, P. Schoenherr, C. Sha, Y. Pan, P. Sharma, M. Alexe, and J. Seidel, Anisotropic ion migration and electronic conduction in van der Waals ferroelectric CuInP_2S_6 , *Nano letters* **21**, 995 (2021).
- ³ M. Checa, X. Jin, R. Millan-Solsona, S. M. Neumayer, M. A. Susner, M. A. McGuire, A. O'Hara, G. Gomila, P. Maksymovych, S. T. Pantelides, et al., Revealing Fast Cu-Ion Transport and Enhanced Conductivity at the CuInP_2S_6 - $\text{In}_{4/3}\text{P}_2\text{S}_6$ Heterointerface, *ACS Nano* **16**, 15347 (2022).
- ⁴ L. You, Y. Zhang, S. Zhou, A. Chaturvedi, S. A. Morris, F. Liu, L. Chang, D. Ichinose, H. Funakubo, W. Hu, et al., Origin of giant negative piezoelectricity in a layered van der Waals ferroelectric, *Science Advances* **5**, eaav3780 (2019).
- ⁵ J. Deng, Y. Liu, M. Li, S. Xu, Y. Lun, P. Lv, T. Xia, P. Gao, X. Wang, and J. Hong, Thickness-Dependent In-Plane Polarization and Structural Phase Transition in van der Waals Ferroelectric CuInP_2S_6 , *Small* **16**, 1904529 (2020).
- ⁶ S. M. Neumayer, E. A. Eliseev, M. A. Susner, A. Tselev, B. J. Rodriguez, J. A. Brehm, S. T. Pantelides, G. Panchapakesan, S. Jesse, and S. V. Kalinin, Giant negative electrostriction and dielectric tunability in a van der Waals layered ferroelectric, *Physical Review Materials* **3**, 024401 (2019).
- ⁷ S. Zhou, L. You, A. Chaturvedi, S. A. Morris, J. S. Herrin, N. Zhang, A. Abdelsamie, Y. Hu, J. Chen, and Y. Zhou, Anomalous polarization switching and permanent retention in a ferroelectric ionic conductor, *Materials Horizons* **7**, 263 (2020).
- ⁸ D.-D. Xu, R.-R. Ma, Y.-F. Zhao, Z. Guan, Q.-L. Zhong, R. Huang, P.-H. Xiang, N. Zhong, and C.-G. Duan, Unconventional out-of-plane domain inversion via in-plane ionic migration in a van der Waals ferroelectric, *Journal of Materials Chemistry C* **8**, 6966 (2020).

- ⁹ W. Ming, B. Huang, S. Zheng, Y. Bai, J. Wang, J. Wang, and J. Li, Flexoelectric engineering of van der Waals ferroelectric CuInP₂S₆, *Science Advances* **8**, eabq1232 (2022).
- ¹⁰ X. Jiang, X. Wang, X. Wang, X. Zhang, R. Niu, J. Deng, S. Xu, Y. Lun, Y. Liu, and T. Xia, Manipulation of current rectification in van der Waals ferroionic CuInP₂S₆, *Nature communications* **13**, 574 (2022).
- ¹¹ S. Zhou, L. You, H. Zhou, Y. Pu, Z. Gui, and J. Wang, Van der Waals layered ferroelectric CuInP₂S₆: physical properties and device applications, *Frontiers of Physics* **16**, 13301 (2021).
- ¹² I. P. Studenyak, V. V. Mitrovciij, G. S. Kovacs, M. I. Gurzan, O. A. Mykajlo, Y. M. Vysochanskii, and V. B. Cajipe, Disordering effect on optical absorption processes in CuInP₂S₆ layered ferrielectrics, *physica status solidi (b)* **236**, 678 (2003).
- ¹³ F. Liu, L. You, K. L. Seyler, X. Li, P. Yu, J. Lin, X. Wang, J. Zhou, H. Wang, H. He, et al., Room-temperature ferroelectricity in CuInP₂S₆ ultrathin flakes, *Nature Communications* **7**, 12357 (2016).
- ¹⁴ W. Huang, F. Wang, L. Yin, R. Cheng, Z. Wang, M. G. Sendeku, J. Wang, N. Li, Y. Yao, and J. He, Gate-Coupling-Enabled Robust Hysteresis for Nonvolatile Memory and Programmable Rectifier in Van der Waals Ferroelectric Heterojunctions, *Adv. Mater.* **32**, 1908040 (2020).
- ¹⁵ X. Wang, P. Yu, Z. Lei, C. Zhu, X. Cao, F. Liu, L. You, Q. Zeng, Y. Deng, C. Zhu, et al., Van der Waals negative capacitance transistors, *Nature Communications* **10**, 3037 (2019).
- ¹⁶ S. M. Neumayer, L. Tao, A. O'Hara, M. A. Susner, M. A. McGuire, P. Maksymovych, S. T. Pantelides, and N. Balke, The Concept of Negative Capacitance in Ionically Conductive Van der Waals Ferroelectrics, *Advanced Energy Materials* **10**, 2001726 (2020).
- ¹⁷ B. Li, S. Li, H. Wang, L. Chen, L. Liu, X. Feng, Y. Li, J. Chen, X. Gong, and K.-W. Ang, An Electronic Synapse Based on 2D Ferroelectric CuInP₂S₆, *Advanced Electronic Materials* **6**, 2000760 (2020).
- ¹⁸ H. Zhu, J. Li, Q. Chen, W. Tang, X. Fan, F. Li, and L. Li, Highly Tunable Lateral Homojunction Formed in Two-Dimensional Layered CuInP₂S₆ via In-Plane Ionic Migration, *ACS Nano* **17**, 1239 (2023).

- ¹⁹ F. Kong, L. Zhang, T. Cong, Z. Wu, K. Liu, C. Sun, L. Pan, and D. Li, Tunable photochemical deposition of silver nanostructures on layered ferroelectric CuInP₂S₆, *Journal of Applied Physics* **132**, 044103 (2022).
- ²⁰ Y. Li, J. Fu, X. Mao, C. Chen, H. Liu, M. Gong, and H. Zeng, Enhanced bulk photovoltaic effect in two-dimensional ferroelectric CuInP₂S₆, *Nature Communications* **12**, 5896 (2021).
- ²¹ Z. Zhao, K. Xu, H. Ryu, and W. Zhu, Strong Temperature Effect on the Ferroelectric Properties of CuInP₂S₆ and Its Heterostructures, *ACS Applied Materials Interfaces* **12**, 51820 (2020).
- ²² S. M. Neumayer, J. A. Brehm, L. Tao, A. O'Hara, P. Ganesh, S. Jesse, M. A. Susner, M. A. McGuire, S. T. Pantelides, P. Maksymovych, et al., Local Strain and Polarization Mapping in Ferrielectric Materials, *ACS Applied Materials & Interfaces* **12**, 38546 (2020).
- ²³ J. Song, Z. Xiao, B. Chen, S. Prockish, X. Chen, A. Rajapitamahuni, L. Zhang, J. Huang, and X. Hong, Enhanced piezoelectric response in hybrid lead halide perovskite thin films via interfacing with ferroelectric PbZr_{0.2}Ti_{0.8}O₃, *ACS Applied Materials Interfaces* **10**, 19218 (2018).
- ²⁴ Z. Hu, M. Tian, B. Nysten, and A. M. Jonas, Regular arrays of highly ordered ferroelectric polymer nanostructures for non-volatile low-voltage memories, *Nature Materials* **8**, 62 (2009).
- ²⁵ Z. Zhao, V. Buscaglia, M. Viviani, M. T. Buscaglia, L. Mitoseriu, A. Testino, M. Nygren, M. Johnsson, and P. Nanni, Grain-size effects on the ferroelectric behavior of dense nanocrystalline BaTiO₃ ceramics, *Physical Review B* **70**, 024107 (2004).
- ²⁶ Y. Noguchi, M. Miyayama, and T. Kudo, Effect of Bi substitution at the Sr site on the ferroelectric properties of dense strontium bismuth tantalate ceramics, *Journal of Applied Physics* **88**, 2146 (2000).
- ²⁷ Y. Hao, T. Li, Y. Yun, X. Li, X. Chen, J. Song, Z. Ahmadi, J. E. Shield, X. Xu, and X. Hong, Tuning Negative Capacitance in PbZr_{0.2}Ti_{0.8}O₃/SrTiO₃ Heterostructures via Layer Thickness Ratio, *Physical Review Applied* **16**, 034004 (2021).
- ²⁸ K. Wang, Y. Hao, L. Zhang, Y. Zhang, X. Chen, and X. Hong, Effect of correlated oxide electrodes on disorder pinning and thermal roughening of ferroelectric domain walls in epitaxial PbZr_{0.2}Ti_{0.8}O₃ thin films, *Physical Review Materials* **5**, 074402 (2021).

- ²⁹ M. Chyasnachyus, M. A. Susner, A. V. Ievlev, E. A. Eliseev, S. V. Kalinin, N. Balke, A. N. Morozovska, M. A. McGuire, and P. Maksymovych, Size-effect in layered ferrielectric CuInP_2S_6 , *Applied Physics Letters* **109**, 172901 (2016).
- ³⁰ L. Chen, Y. Li, C. Li, H. Wang, Z. Han, H. Ma, G. Yuan, L. Lin, Z. Yan, and X. Jiang, Thickness dependence of domain size in 2D ferroelectric CuInP_2S_6 nanoflakes, *AIP Advances* **9**, 115211 (2019).
- ³¹ S. Li, J. A. Eastman, Z. Li, C. M. Foster, R. E. Newnham, and L. E. Cross, Size effects in nanostructured ferroelectrics, *Physics Letters A* **212**, 341 (1996).
- ³² M. A. Susner, M. Chyasnachyus, A. A. Puretzky, Q. He, B. S. Conner, Y. Ren, D. A. Cullen, P. Ganesh, D. Shin, and H. Demir, Cation–eutectic transition via sublattice melting in $\text{CuInP}_2\text{S}_6/\text{In}_{4/3}\text{P}_2\text{S}_6$ van der Waals layered crystals, *ACS nano* **11**, 7060 (2017).
- ³³ L. D. Landau and E. M. Lifshitz, *Statistical Physics: Volume 5* (Elsevier, 2013).
- ³⁴ R. Fei, W. Kang, and L. Yang, Ferroelectricity and phase transitions in monolayer group-IV monochalcogenides, *Physical review letters* **117**, 097601 (2016).
- ³⁵ N. Sivadas, P. Doak, and P. Ganesh, Anharmonic stabilization of ferrielectricity in $\text{CuInP}_2\text{Se}_6$, *Physical Review Research* **4**, 013094 (2022).
- ³⁶ X. Chen, X. Zhang, M. A. Koton, H. Chen, Z. Xiao, L. Zhang, J. E. Shield, P. A. Dowben, and X. Hong, Interfacial Charge Engineering in Ferroelectric-Controlled Mott Transistors, *Advanced Materials* **29**, 1701385 (2017).
- ³⁷ N. Pertsev, V. Kukhar, H. Kohlstedt, and R. Waser, Phase diagrams and physical properties of single-domain epitaxial $\text{Pb}(\text{Zr}_{1-x}\text{Ti}_x)\text{O}_3$ thin films, *Physical Review B* **67**, 054107 (2003).
- ³⁸ J. P. Killgore, L. Robins, and L. Collins, Electrostatically-blind quantitative piezoresponse force microscopy free of distributed-force artifacts, *Nanoscale Advances* **4**, 2036 (2022).
- ³⁹ P. E. Blöchl, Projector augmented-wave method, *Physical Review B* **50**, 17953 (1994).
- ⁴⁰ G. Kresse and J. Furthmüller, Efficient iterative schemes for ab initio total-energy calculations using a plane-wave basis set, *Physical review B* **54**, 11169 (1996).
- ⁴¹ J. P. Perdew, K. Burke, and M. Ernzerhof, Generalized Gradient Approximation Made Simple, *Physical Review Letters* **77**, 3865 (1996).

- ⁴² P. Gao, H.-J. Liu, Y.-L. Huang, Y.-H. Chu, R. Ishikawa, B. Feng, Y. Jiang, N. Shibata, E.-G. Wang, and Y. Ikuhara, Atomic mechanism of polarization-controlled surface reconstruction in ferroelectric thin films, *Nature Communications* **7**, 11318 (2016).
- ⁴³ D. Akbarian, D. E. Yilmaz, Y. Cao, P. Ganesh, I. Dabo, J. Munro, R. Van Ginhoven, and A. C. T. van Duin, Understanding the influence of defects and surface chemistry on ferroelectric switching: a ReaxFF investigation of BaTiO₃, *Physical Chemistry Chemical Physics* **21**, 18240 (2019).
- ⁴⁴ X. Hong, J. Hoffman, A. Posadas, K. Zou, C. H. Ahn, and J. Zhu, Unusual resistance hysteresis in n-layer graphene field effect transistors fabricated on ferroelectric Pb(Zr_{0.2}Ti_{0.8})O₃, *Applied Physics Letters* **97**, 033114 (2010).
- ⁴⁵ M. E. J. Newman and G. T. Barkema, *Monte Carlo methods in statistical physics* (Clarendon Press, Oxford, 1999).

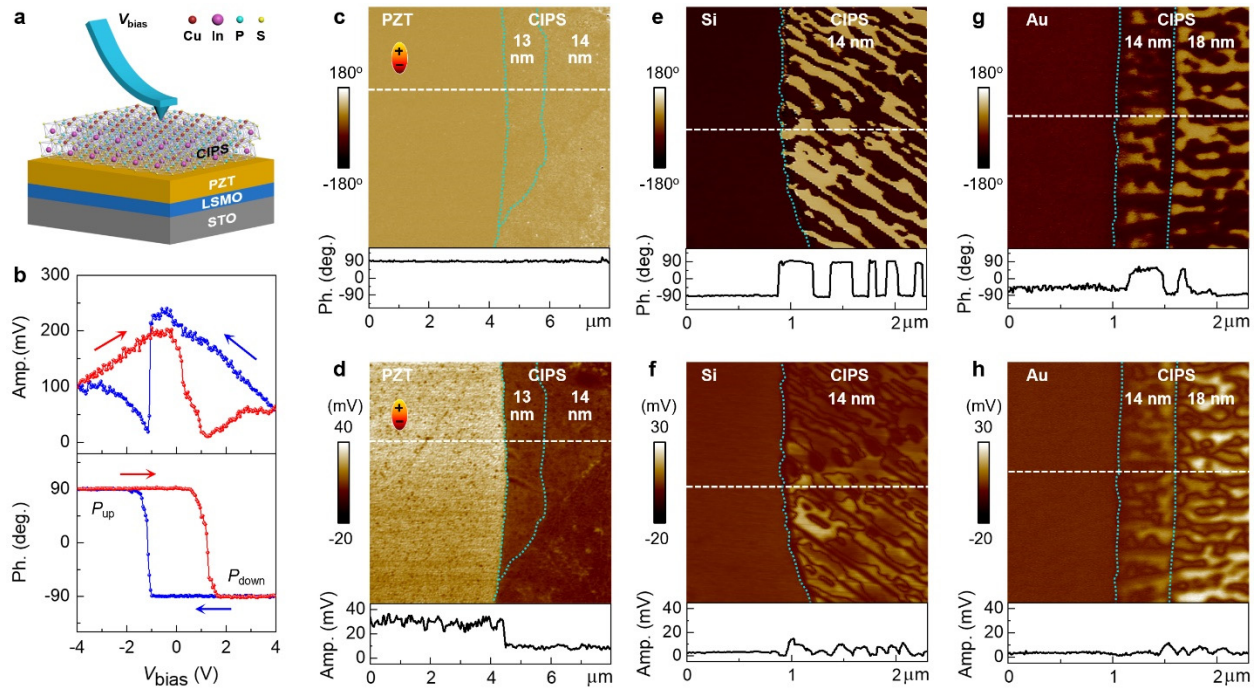


Figure 1. Effect of base layer on domain formation in 14 nm CIPS. (a) Schematic experimental setup. (b) PFM amplitude (top) and phase (bottom) switching hysteresis taken on a 50 nm PZT. (c)-(d) PFM phase (c) and amplitude (d) images taken on 13-14 nm CIPS on P_{up} domain of PZT. (e)-(f) PFM phase (e) and amplitude (f) images taken on 14 nm CIPS on Si. (g)-(h) PFM phase (g) and amplitude (h) images taken on 14-18 nm CIPS on Au. The lower panels in (c)-(h) show the cross-sectional signal profiles along the dashed lines. The dotted lines illustrate the edges of CIPS.

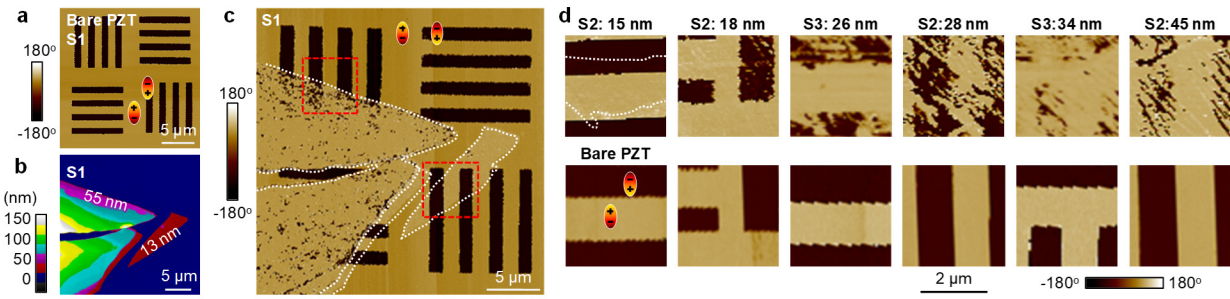


Figure 2. Effect of t_{CIPS} on domain formation in CIPS on PZT. (a) PFM phase image of pre-patterned domains in PZT/LSMO (S1). (b)-(c) AFM topography (b) and PFM phase (c) images of sample S1 with CIPS transferred on top. The CIPS flake thickness is indicated in (b). The dashed boxes outline the regions discussed in Figure 5a,c. (d) PFM phase images taken on samples S2 and S3. Upper panels: CIPS with different thicknesses on pre-patterned domains of PZT. Lower panels: The corresponding domain structures on bare PZT before CIPS transfer. The dotted lines in (c) and (d) outline the CIPS flakes. For bare PZT, the bright (dark) regions correspond to the P_{up} (P_{down}) states.

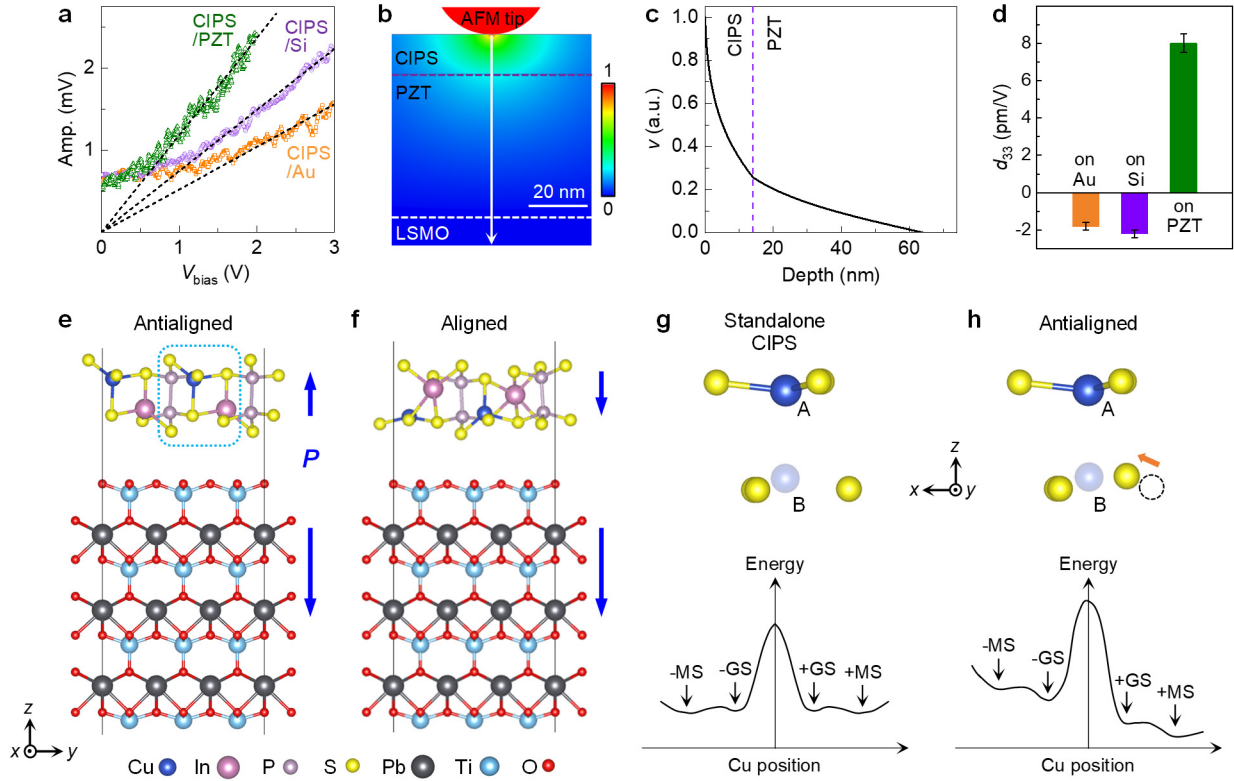


Figure 3. Analysis of d_{33} and polar alignment of CIPS. (a) PFM amplitude vs V_{bias} taken on the CIPS samples shown in Figure 1c-h, with linear fits (dashed lines). (b) Simulated distribution of normalized V_{bias} (v) across a 14 nm CIPS/50 nm PZT/10 nm LSMO stack, and (c) v along the vertical arrow in (b). The dashed lines indicate the interfaces. (d) Averaged d_{33} for 14 nm CIPS flakes on three types of base layers. (e)-(f) DFT modeling of the crystal structures of relaxed CIPS on PTO frozen in the P_{down} state, with CIPS in the P_{up} (e) and P_{down} (f) states. The arrows indicate the polarization (P) directions. (g)-(h) Schematics of sulfur and copper ion arrangements (upper panel) and ferroelectric quadruple-well energy profiles (lower panel) for standalone CIPS (g) and CIPS on P_{down} state of PTO (h). The crystal structure in (h) illustrates the boxed area in (e). The arrow in (h) indicates the shift of sulfur ion relative to its position in (g) (dashed circle). A and B correspond to the Copper ion positions in the P_{up} and P_{down} states, respectively.

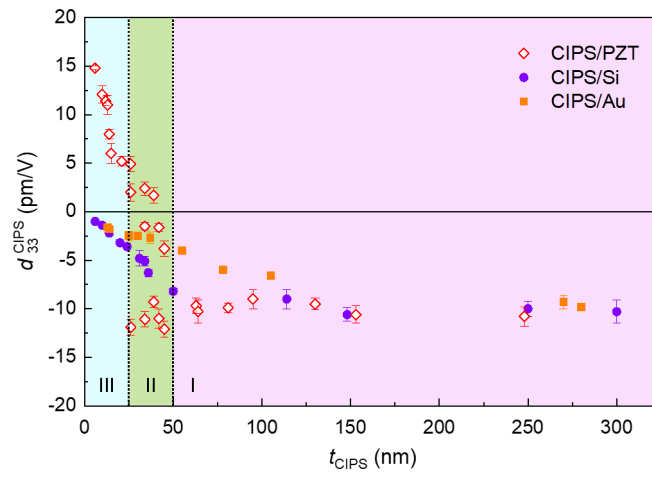


Figure 4. CIPS thickness dependence of d_{33}^{CIPS} . d_{33}^{CIPS} vs t_{CIPS} for CIPS on different base layers.

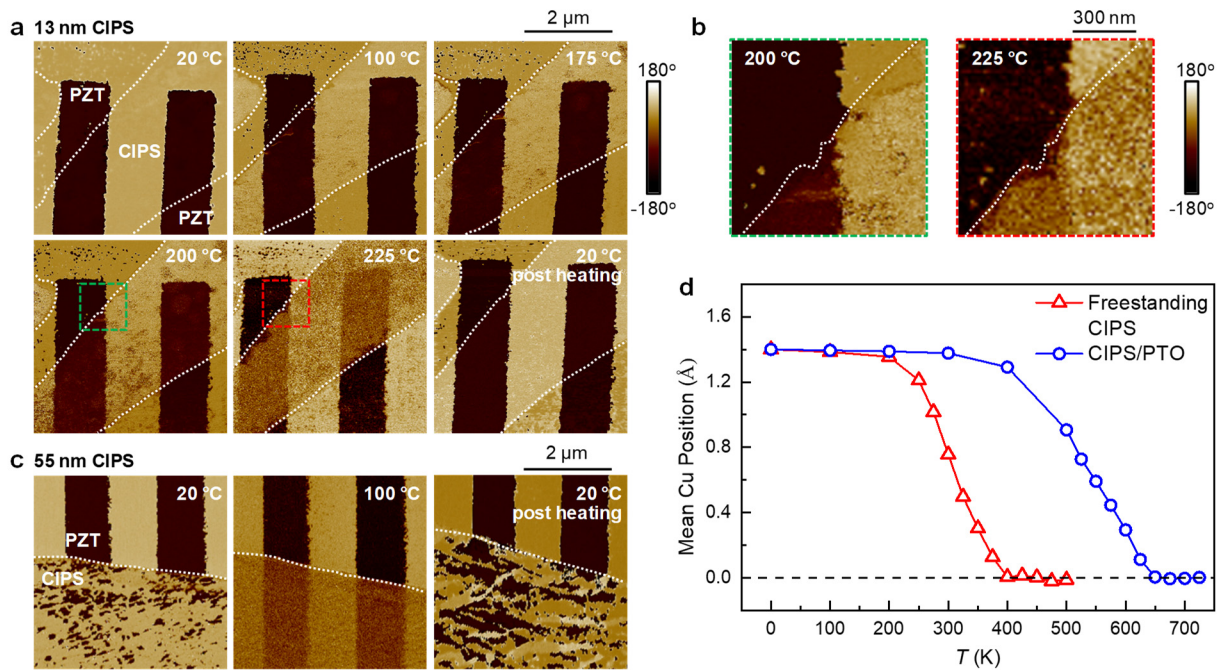


Figure 5. Enhanced T_C for CIPS on PZT. (a)-(c) *In situ* PFM phase images at selected temperatures taken on sample S1 for the 13 nm (a)-(b) and 55 nm (c) CIPS regions outlined in Figure 2(c). The images in (b) are the expanded views of the boxed areas in (a). The dotted lines illustrate the CIPS/PZT boundaries. All images have the same color scale bars. (d) Monte Carlo simulations of mean Cu position at different temperatures.

Interface-tuning of ferroelectricity and quadruple-well state in CuInP_2S_6 via ferroelectric oxide (Supporting Information)

Kun Wang¹, Du Li², Jia Wang¹, Yifei Hao¹, Hailey Anderson¹, Li Yang², and Xia Hong^{*1}

¹ *Department of Physics and Astronomy & Nebraska Center for Materials and Nanoscience, University of Nebraska-Lincoln, Lincoln, Nebraska 68588-0299, USA*

² *Department of Physics, Washington University in St. Louis, St. Louis, Missouri 63130-4899, USA*

* Email: xia.hong@unl.edu

Section 1: Characterization of Base Layers

Figure S1a shows the x-ray diffraction (XRD) θ - 2θ scan taken on a 50 nm $\text{PbZr}_{0.2}\text{Ti}_{0.8}\text{O}_3$ (PZT)/10 nm $\text{La}_{0.67}\text{Sr}_{0.33}\text{MnO}_3$ (LSMO) heterostructure deposited on (001) SrTiO_3 substrate, which reveals (001) growth with no impurity phases. The Laue oscillation around the Bragg peak confirms the high crystallinity of the sample. Atomic force microscopy (AFM) measurements of the PZT (Figure S1b), doped Si (Figure S1c), and Au (Figure S1d) base layers show smooth surfaces with the root-mean-square (RMS) roughness $\leq 5 \text{ \AA}$.

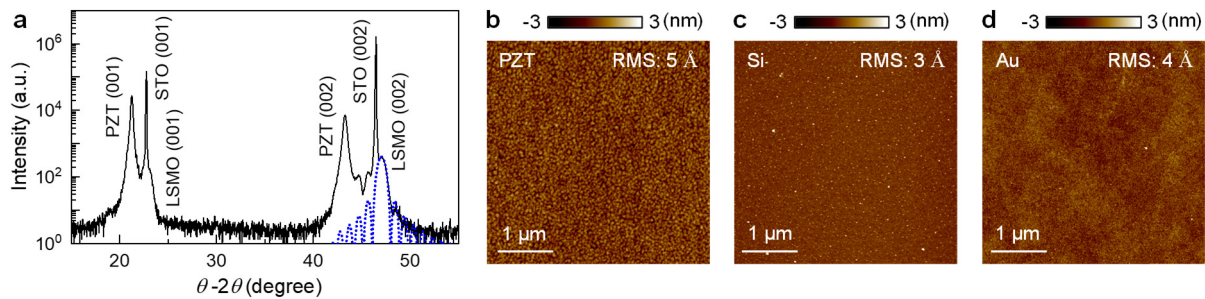


Figure S1. Structure and surface characterizations of PZT, Si, and Au base layers. (a) XRD θ - 2θ scan of a 50 nm PZT/10 nm LSMO deposited on SrTiO_3 . The blue dotted line is a fit to the Laue oscillation

around the (002) Bragg peak of LSMO. (b)-(d) AFM topography images taken on PZT (b), doped Si (c), and 10 nm Au/2 nm Ti deposited on Si (d).

We write square polarization up (P_{down}) and down (P_{up}) domains on a bare PZT film using the conductive probe AFM. As shown in the PFM phase (Figure S2a) and amplitude (Figure S2b) images, the as grown film is uniformly polarized in the P_{up} state.

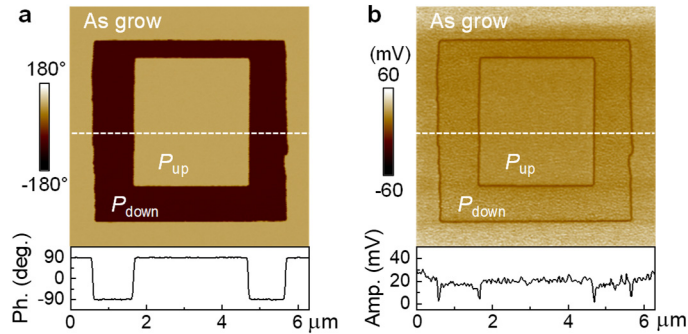


Figure S2. PFM characterizations of PZT/LSMO. (a) PFM phase and (d) amplitude images of concentric square domains. The P_{down} (P_{up}) dashed box in (a) indicates the domain writing area with $V_{\text{bias}} = 4 \text{ V}$ ($V_{\text{bias}} = -4 \text{ V}$). The lower panels show the signal profiles along the dashed lines.

Figure S3 shows the AFM topography images of the 14 nm CuInP_2S_6 (CIPS) flakes on different base layers. The piezoresponse force microscopy (PFM) images of these flakes are shown in the main text Figure 1c-h.

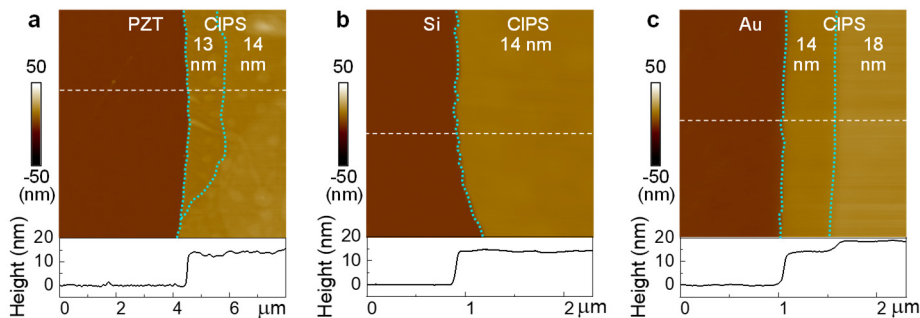


Figure S3. AFM measurements of 14 nm CIPS on different base layers. (a)-(c), AFM topography images of CIPS flakes on PZT P_{up} domain (a), Si (b), and Au (c). The lower panels show the cross-sectional signal profiles along the dashed lines. The dotted lines illustrate the edges of CIPS.

Section 2: CIPS on Prepatterned Domain Structures in PZT

Using conductive AFM, we create on PZT a series of rectangular P_{down} domains in a uniformly polarized P_{up} background and transfer CIPS flakes on top. Figure S4 shows the PFM amplitude images taken on sample S1 before and after the CIPS transfer.

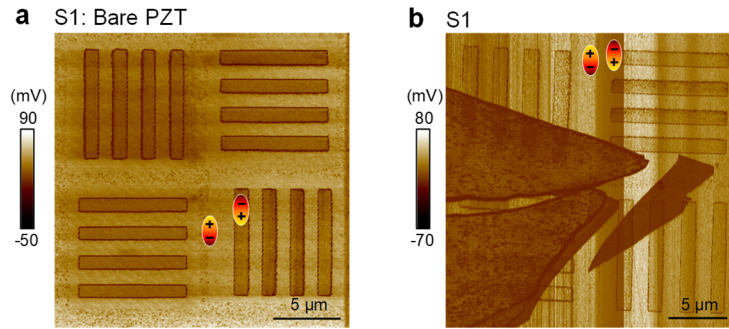


Figure S4. Characterization of sample S1. (a) PFM amplitude image of prepatterned domains in bare PZT/LSMO (S1). (b) PFM amplitude image of the same area with CIPS transferred on top. The corresponding AFM topography and PFM phase images are shown in the main text Figure 2a-c.

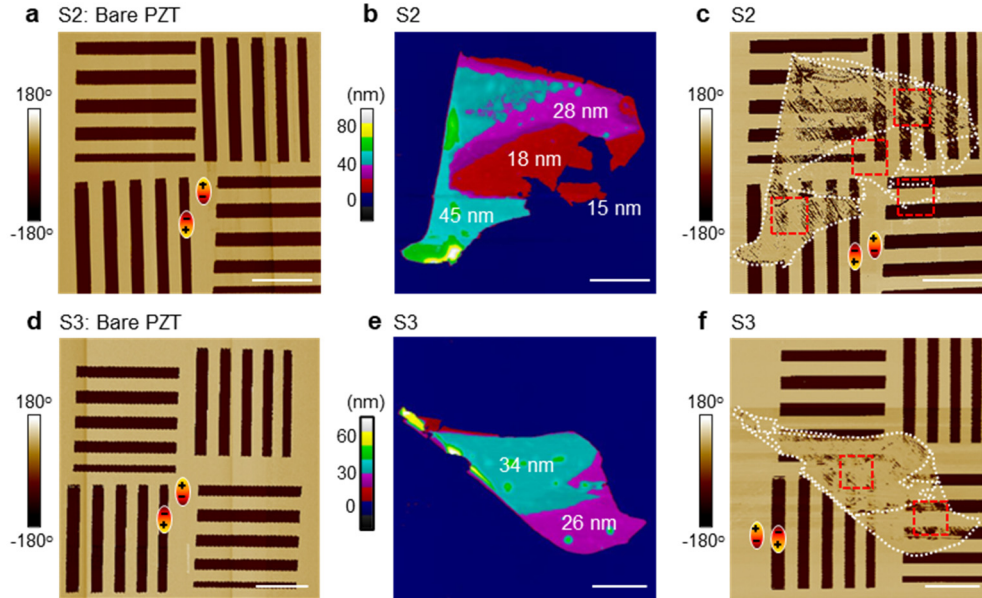


Figure S5. Characterization of samples S1 and S2. (d)-(f) AFM and PFM images for CIPS/PZT sample S3. (a) PFM phase image of prepatterned domains in bare PZT/LSMO. (b) AFM and (c) PFM phase images of the same area with CIPS transferred on top. (d)-(f) AFM and PFM images for CIPS/PZT sample S3. (d) PFM phase image of prepatterned domains in bare PZT/LSMO. (e) AFM and (f) PFM

phase images of the same area with CIPS transferred on top. The red dashed boxes in (c) and (f) outline the areas shown in the main text Figure 2d. The scale bars represent 5 μm in all images.

Figure S5a shows the PFM phase image of the prepatterned domain structure taken on bare PZT for sample S2. The AFM and PFM phase images of the same area with a CIPS flake transferred on top are shown in Figure S5b-c, respectively. Figure S5d-f shows the AFM and PFM characterizations of sample S3. Figure S6 shows the PFM amplitude images for the boxed areas in Figure S5c,f. The corresponding phase images are shown in the main text Figure 2d.

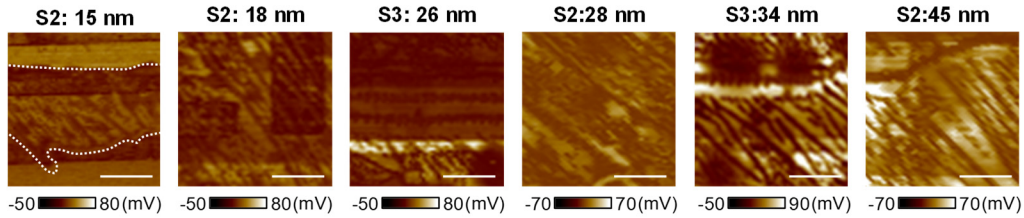


Figure S6. PFM amplitude images of the boxed areas in Figure S5c,f. The dotted lines outline the CIPS/PZT boundary. The scale bars represent 2 μm in all images.

Section 3: Analysis of Piezoelectric Coefficient

We characterize the effective piezoelectric coefficient d_{33} by performing off-resonance PFM ramping using the Bruker SCM-PIT-V2 probe (spring constant: 3 N/m; tip radius: ~ 25 nm; free-space resonant frequency: ~ 75 kHz). The tip deflection sensitivity is calibrated by performing the force ramping before each measurement. The tip deflection sensitivity $S = 54$ nm/V is extracted from the force curve (deflection vs tip height) with $S = 1/\text{slope}$ (Figure S7a). We ground the sample bottom electrode, apply an AC bias (V_{bias}) at the sweeping rate of 0.1 V/s to the tip, and measure the corresponding piezoresponse. Figure S7b shows the PFM amplitude vs V_{bias} taken at frequencies of 10-60 kHz for V_{bias} , which are well below the cantilever's free-space resonant frequency. There is less than 10% variation in the slope at the frequency range of 20-60 kHz, showing that the result is robust and frequency-independent. The signals taken at 10 kHz are very

noisy. We use 40 kHz for all d_{33} measurements in the main text for the optimized signal-to-noise ratio. From the PFM ramping curves (Figure S7c), we extract d_{33} of 40 ± 0.1 pm/V for the P_{up} state and 37 ± 0.1 pm/V for the P_{down} state of PZT. We use the average value of $d_{33}^{\text{PZT}} = 39 \pm 2$ pm/V for PZT in analyzing the piezoresponse of CIPS.

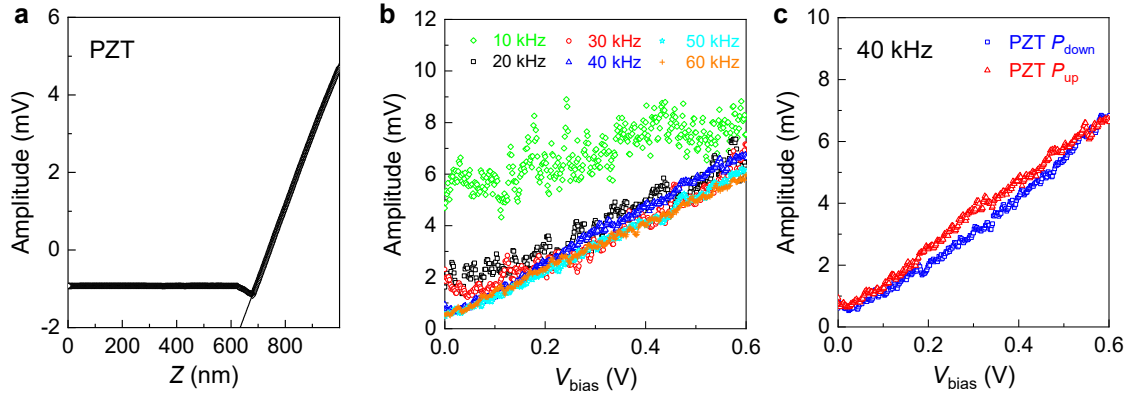


Figure S7. Off-resonance PFM ramping measurements of PZT. (a) Deflection amplitude vs tip height with a linear fit (solid line). (b) PFM amplitude vs V_{bias} at 10-60 kHz taken on the P_{up} domain of PZT. (c) PFM amplitude vs V_{bias} at 40 kHz taken on P_{up} and P_{down} domains of PZT.

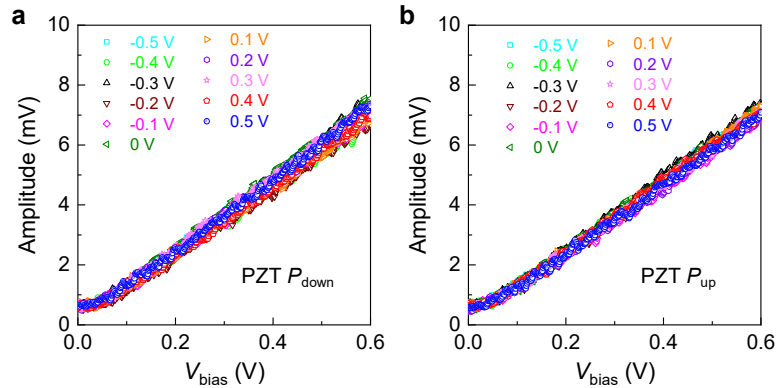


Figure S8. Effect of V_{DC} on off-resonance PFM ramping measurements. PFM amplitude vs V_{bias} with different V_{DC} from -0.5 V to 0.5 V taken on bare PZT prepatterned into (a) P_{down} and (b) P_{up} domains.

We also examine the effect of the electrostatic force on d_{33} measurements by superimposing a DC bias (V_{DC}) when performing PFM ramping measurement.¹ Figure S8 shows the PFM amplitude vs V_{bias} taken on bare PZT P_{down} and P_{up} domains with different external V_{DC} from -0.5 to 0.5 V.

The curves are highly consistent and there is less than 15% variation in the slope with different V_{DC} . These V_{DC} -independent results indicate that our measurements are not affected by the surface electrostatic charges and the obtained piezoresponse of the CIPS/PZT heterostructure is reliable.

To determine the sign of the piezoelectric response of CIPS on Si and Au, we compare their PFM switching hysteresis loops with that of bare PZT. As shown in Figure S9, the PFM phase vs V_{bias} loops for CIPS on Si and Au switch in the counterclockwise direction, while that of bare PZT switches in clockwise direction. Since PZT has a positive d_{33} , we conclude that d_{33} for CIPS on Si and Au is negative.

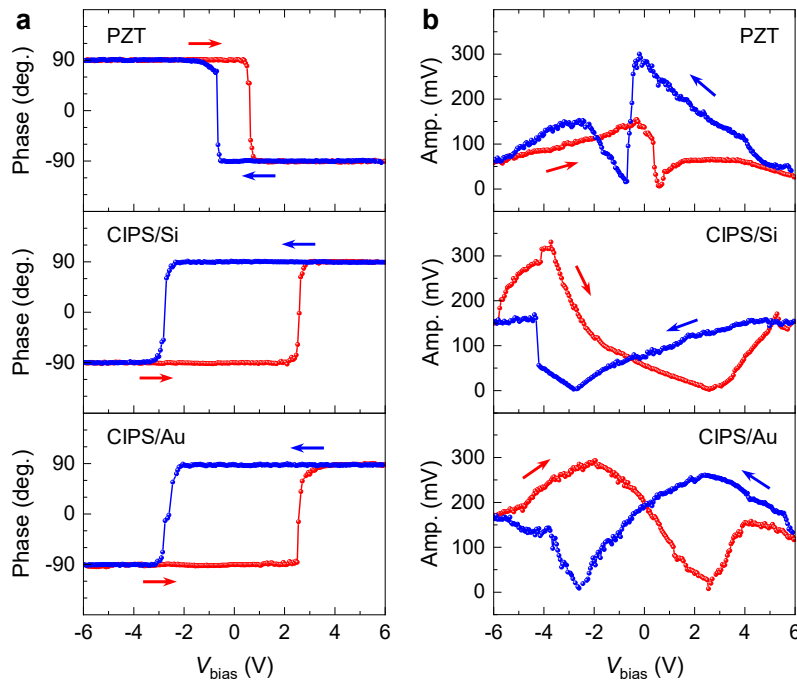


Figure S9. PFM switching hysteresis for bare PZT, CIPS on Si, and CIPS on Au. (a)-(b) PFM phase (a) and amplitude (b) switching hysteresis taken on bare PZT (top panels), 42 nm CIPS on Si (middle panels), and 36 nm CIPS on Au (bottom panels). The arrows label the sweeping directions of V_{bias} .

Section 4: Finite Element Analysis of V_{bias} Distribution in CIPS/PZT Stacks

We perform finite element analysis to calculate the bias voltage distribution across the CIPS/PZT stack (main text, Methods). Figure S10 shows the fractional voltage drop across the

CIPS layer on 50 nm PZT/10 nm LSMO as a function of CIPS thickness t_{CIPS} . The results are used to extract d_{33}^{CIPS} from the net piezoresponse of the CIPS/PZT stack [Equation (1) in the main text]. The finite element analysis results also provide a guide to determine the proper V_{bias} for PFM studies without switching the polarization of the PZT layer.

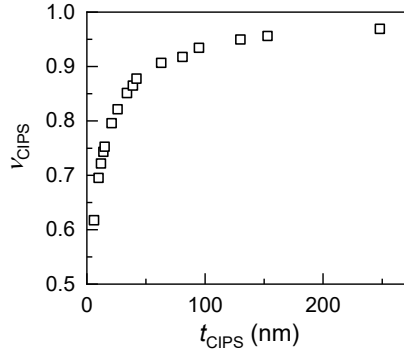


Figure S10. Finite element analysis of voltage distribution across CIPS/PZT. The simulated fractional voltage across the CIPS layer (v_{CIPS}) vs t_{CIPS} for CIPS flakes on 50 nm PZT/10 nm LSMO.

Section 5: Time-Dependent PFM Measurements of CIPS on PZT

We perform time-dependent PFM imaging of the domain structure on PZT after CIPS transfer. Figure S11a shows a series of PFM images taken at different time intervals after domain writing at Hour 0. The initial PFM response of the CIPS regions is fuzzy (Hour 1). As the freshly switched domain surface is highly charged and attracts screening charges from the environment, it can cause charge redistribution in CIPS, which affects its PFM response. After 16 hours, the bound charge of PZT is mostly screened,² and the domain structure in CIPS fully conforms with that in the underlying PZT. Once settled, the domain structure remains stable for over 11 days, which is the measurement duration.

We also characterize d_{33}^{CIPS} for the 10 nm CIPS region on PZT with time. As shown in Figure S11c, d_{33}^{CIPS} increases from 10.8 pm/V at Hour 1 to 12.1 pm/V at Hour 16 and remains stable afterwards. This value is consistent with $d_{33}^{\text{CIPS}} = 12.1 \pm 0.9$ pm/V obtained for the 10 nm CIPS

transferred after 24 hours of domain writing (main text, Figure 4). For the PFM studies reported in the main text, we wait for 24 hours after domain writing in PZT at ambient conditions before the CIPS transfer to ensure a stable electrostatic condition of PZT surface.

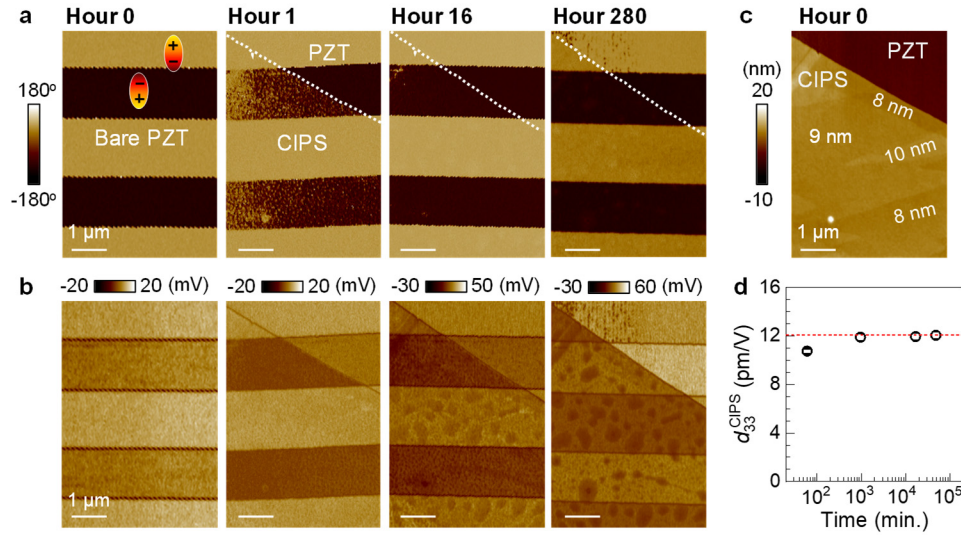


Figure S11. Time-dependent PFM imaging of CIPS on PZT. (a)-(b) PFM phase (a) and amplitude (b) images taken on bare PZT right after domain writing (Hour 0) and taken with a CIPS flake transferred on top after 1, 16, and 280 hours of domain writing. The bright (dark) regions in (a) correspond to P_{up} (P_{down}) states of PZT. (c) AFM topography image of the sample, with flake thickness indicated. All scale bars represent 1 μm . (d) d_{33}^{CIPS} for the 10 nm CIPS region as a function of time after domain writing. The dashed line marks 12.1 pm/V.

Section 6: *In Situ* PFM Imaging of CIPS on Si, Au, and PZT

As a control study, we also examine the Curie temperature (T_C) for 14 nm CIPS on Si and Au base layers. We heat the CIPS/Si and CIPS/Au samples at progressive temperatures, wait for 30 minutes after the temperature is stabilized, and then perform *in situ* PFM imaging on the same area. As shown in Figure S12, CIPS on Si exhibits spontaneous stripe domains at room temperature (20 °C). At 50 °C, the PFM phase and amplitude signals start to become blurred, suggesting the sample is approaching T_C . Above 50 °C, clear PFM phase contrast is only observed along the step features

shown in the sample morphology (indicated by the arrows), while the PFM amplitude is substantially quenched. After cooling back down to 20 °C, new domain structures emerge, further indicating that the CIPS sample has been cycled through T_c .

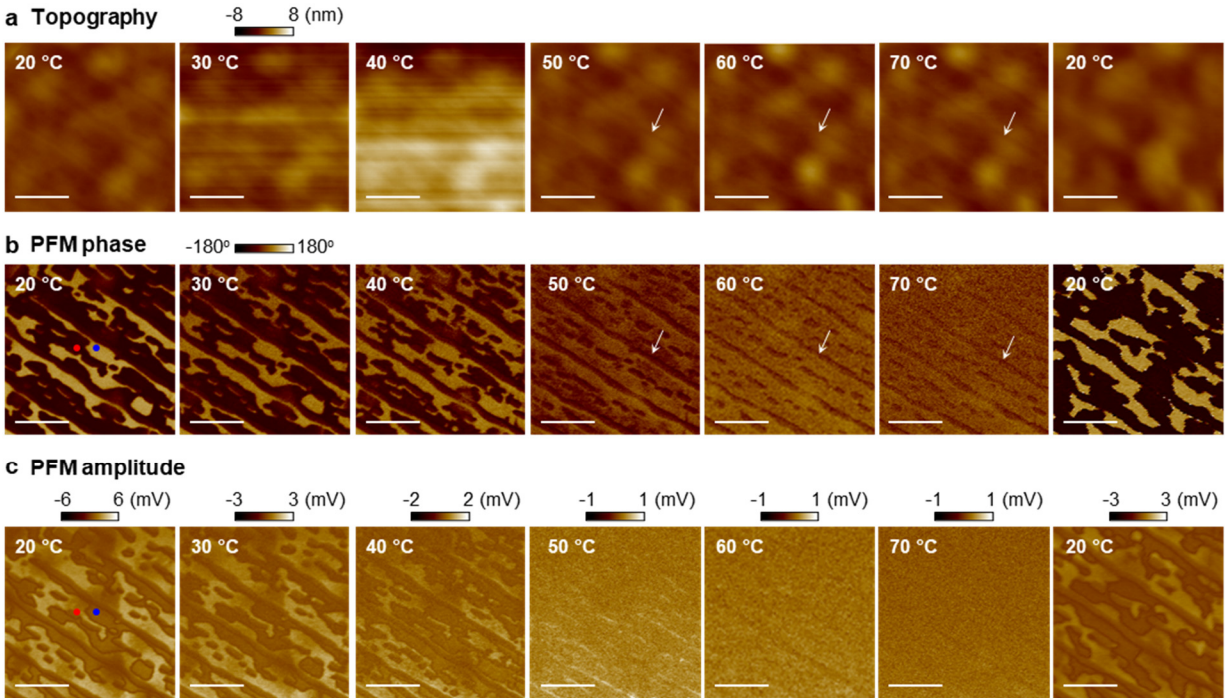


Figure S12. *In situ* PFM imaging of CIPS on Si. (a)-(c) *In situ* AFM (a), PFM phase (b), and PFM amplitude (c) images taken on 14 nm CIPS flakes on Si at selected temperatures through thermal cycling. All images in (a) and (b) have the same height and phase signal scales, respectively. The arrows in (a) and (b) indicate the step feature in the topography image and the corresponding PFM phase contrast, respectively. All scale bars represent 500 nm.

Figure S13a-b shows the PFM phase and amplitude signal, respectively, taken on the P_{down} and P_{up} domains of CIPS (labeled positions in Figure S12b-c) at different temperatures. The phase signals for the P_{up} and P_{down} states approach the same value at 60 °C, suggesting the annihilation of domains. The amplitude signal is also quenched at temperatures above 50 °C. We thus conclude that T_c for the 14 nm CIPS on Si is between 50 and 60 °C.

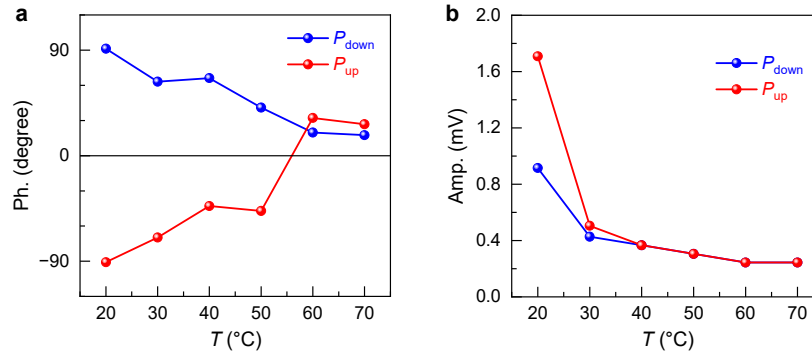


Figure S13. Temperature dependence of PFM signal for CIPS on Si. (a)-(b) *In situ* PFM phase (a) and amplitude (b) signal vs temperature for the P_{up} and P_{down} states taken at the positions marked by the red and blue dots, respectively, in Figure S12.

Similar temperature evolution of the domain structure has been observed in the 14 nm CIPS on Au. As shown in Figure S14, the domain structures remain stable till 50 °C and become blurred at 60 °C. When heated to 70 °C, the domains completely disappear. After cooling back down to 20 °C, new domain structures emerge, further confirming that the sample has been cycled through T_C .

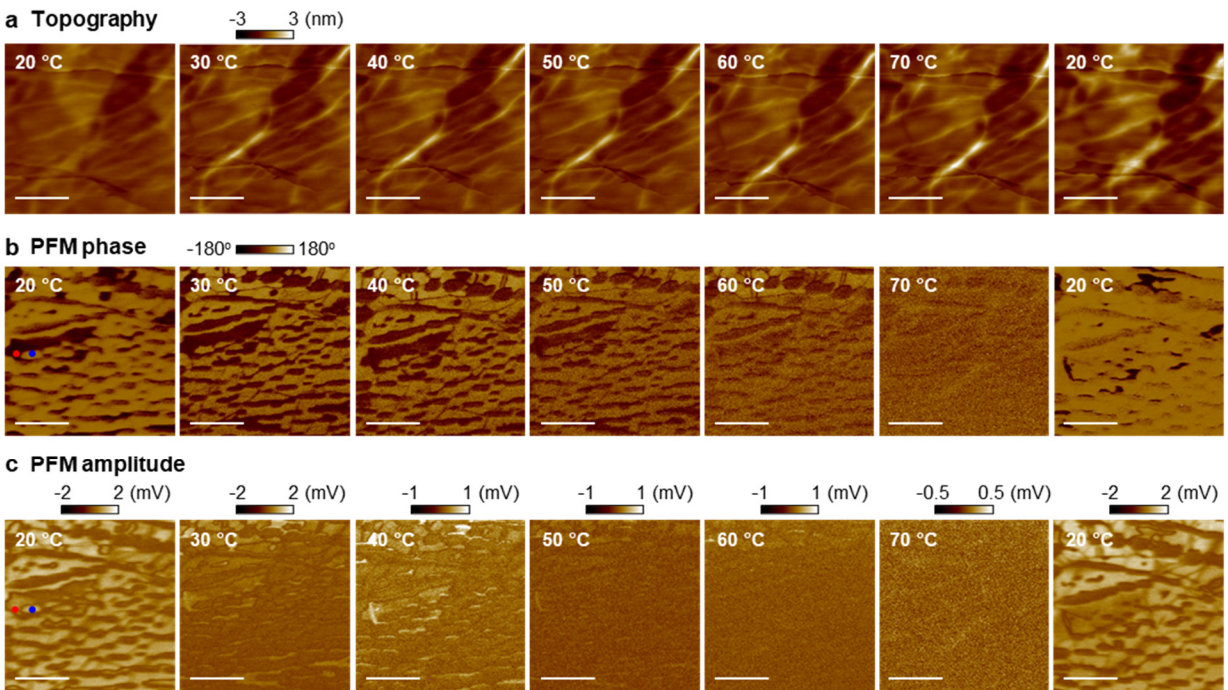


Figure S14. *In situ* PFM imaging of CIPS on Au. (a)-(c) *In situ* AFM (a), PFM phase (b), and PFM amplitude (c) images taken on 14 nm CIPS flakes on Au at selective temperatures through the thermal

cycling. All images in (a) and (b) have the same height and phase signal scales, respectively. All scale bars represent 500 nm.

As shown in Figure S15, the PFM phase signal for the P_{up} and P_{down} states for this sample approaches the same value at 60 °C. We thus conclude that T_C for the 14 nm CIPS on Au is also between 50 and 60 °C.

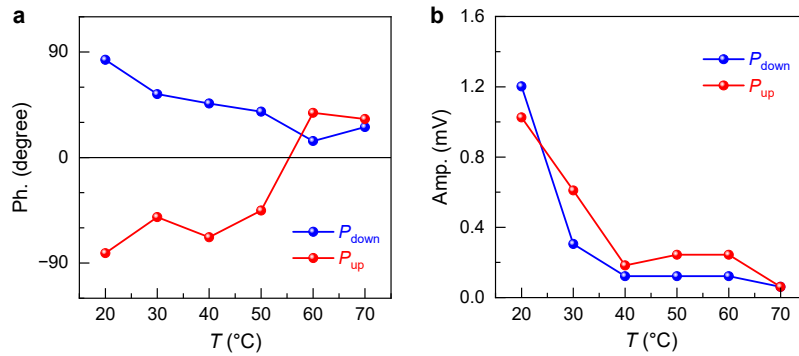


Figure S15. Temperature dependence of PFM signal for CIPS on Au. (a)-(b) *In situ* PFM phase (a) and amplitude (b) signal vs temperature for the P_{up} and P_{down} states taken at the positions marked by the red and blue dots, respectively, in Figure S14.

Figure S16 shows the *in situ* PFM amplitude images at selected temperatures taken on the 13 nm and 55 nm regions of CIPS in sample S1.

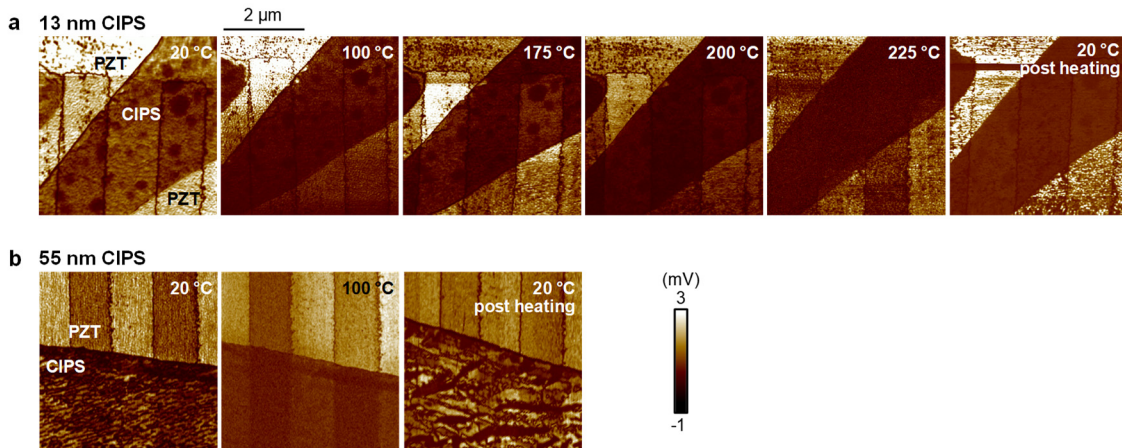


Figure S16. *In situ* PFM imaging of CIPS on PZT. (a)-(b) *In situ* PFM amplitude images at selected temperatures taken on sample S1 for the 13 nm (a) and 55 nm (b) CIPS regions. The corresponding

PFM phase images are shown in Figure 5 in the main text. All images have the same length and height scale bars.

Section 7: Theoretical Modeling

We calculate the energy barrier for Cu atom displacement using the Nudged Elastic Band (NEB) method. The results are shown in Figure S17. We then fit the free energy double-well within the Landau theory using a 6th-order polynomial: $E = ax^2 + bx^4 + cx^6$, where x is the Cu displacement.^{3,4} The fitting parameters are listed in Table S1. The energy barrier per Cu atom is 214 meV for standalone CIPS. In contrast, the energy barrier is enhanced to 374 meV for CIPS on PbTiO₃ (PTO), which yields a higher T_C of CIPS. Using Landau theory,³ we estimate the enhancement of T_C by comparing the ratios of b/a for the two double-well energy fittings. The result shows that T_C for CIPS on PTO is 42% larger than that for standalone CIPS.

We note that the ferroelectric double well for CIPS/PTO is not symmetric. For CIPS on PTO in the P_{down} state, the energy minimum for Cu upward displacement is 25 meV lower than that of downward displacement. It indicates that the P_{up} orientation of CIPS is energetically more favorable for CIPS on the P_{down} state of PTO, or the polarization of CIPS and PTO prefers to be antialigned. Since the 25 meV variation is much smaller than the energy barrier, we can still use the symmetrical polynomial fit in the Monte Carlo simulation.

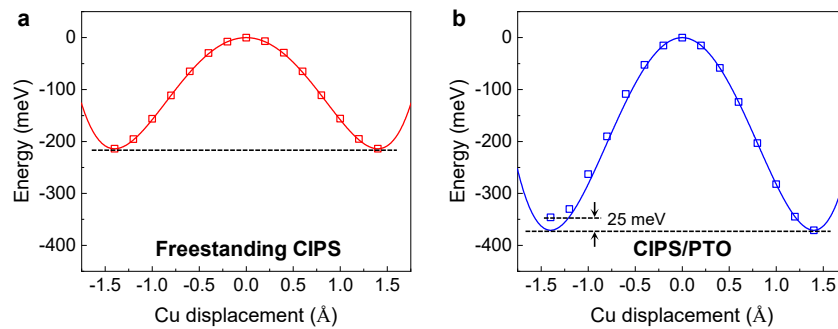


Figure S17. DFT modeling of CIPS free energy. (a)-(b) Calculated free energy profile per Cu ion using the NEB method for standalone CIPS (a) and CIPS on PTO in the P_{down} state (b). The solid lines indicate

the polynomial fits to the symmetric energy double well. The positive (negative) Cu displacement corresponds to the upward (downward) direction.

	a (meV Å ⁻²)	b (meV Å ⁻⁴)	c (meV Å ⁻⁶)	$-b/a$ (Å ⁻²)
Standalone CIPS	-199.26	36.20	4.97	0.18
CIPS on PTO	-379.70	97.71	0.29	0.26

Table S1. Fitting parameters for the ferroelectric double-well energy of CIPS.

To understand the microscopic origin of the preference of antialignment between the polarizations of CIPS and PTO, we calculate the crystal structures of CIPS on PTO. As shown in Figure S18, when the polarizations of CIPS and PTO are antialigned, *i.e.*, P_{up} of CIPS on P_{down} of PTO (Figure S18a), all copper ions in the interfacial CIPS layer are aligned in the same horizontal plane. When the polarizations are aligned, *i.e.*, P_{down} of CIPS on P_{down} of PTO (Figure S18b), on the other hand, there is a larger variation in the position of Cu ions along z -direction. The corresponding standard deviations of Cu displacement for the P_{up} and P_{down} states of CIPS are 0.01 and 0.15 Å, respectively. The larger variation in Cu ion position causes higher lattice distortion and results in a higher elastic energy cost for the P_{down} state. It is thus preferable for CIPS and PTO to have the polarization antialigned.

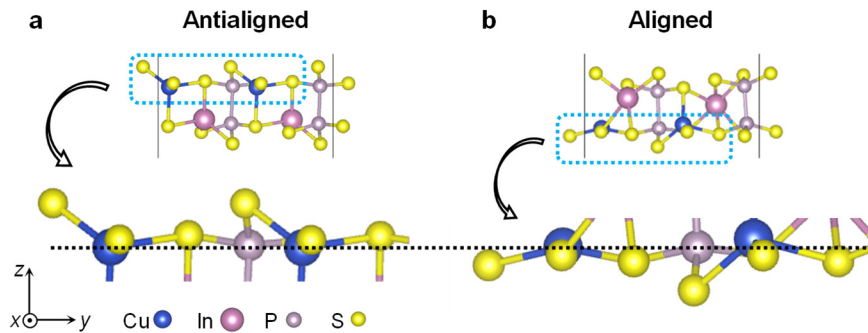


Figure S18. DFT modeling of structural distortion of CIPS on PTO. (a)-(b) Calculated crystal structures for CIPS on P_{down} state of PTO with CIPS polarization antialigned (a) and aligned (b) with

that of PTO. These are the expanded views of Figure 3e-f in the main text. The bottom PTO layer is not shown for simplicity. Lower panels: Expanded views for the boxed areas in the upper panels. The dotted line serves as a guide to the eye.

References

- ¹ J. P. Killgore, L. Robins, and L. Collins, Electrostatically-blind quantitative piezoresponse force microscopy free of distributed-force artifacts, *Nanoscale Advances* **4**, 2036 (2022).
- ² J. Song, Z. Xiao, B. Chen, S. Prockish, X. Chen, A. Rajapitamahuni, L. Zhang, J. Huang, and X. Hong, Enhanced piezoelectric response in hybrid lead halide perovskite thin films via interfacing with ferroelectric $\text{PbZr}_{0.2}\text{Ti}_{0.8}\text{O}_3$, *ACS Applied Materials Interfaces* **10**, 19218 (2018).
- ³ L. D. Landau and E. M. Lifshitz, *Statistical Physics: Volume 5* (Elsevier, 2013).
- ⁴ W. Song, R. Fei, and L. Yang, Off-plane polarization ordering in metal chalcogen diphosphates from bulk to monolayer, *Physical Review B* **96**, 235420 (2017).